



Synthesis of Micro/nanostructured Co_9S_8 Cubes and Spheres as High Performance Anodes for Lithium Ion Batteries



Y.H. Wang, B.H. Wu, X.Y. He, Y.Y. Zhang, H. Li, Y.Y. Peng, J. Wang*, J.B. Zhao*

State Key Laboratory of Physical Chemistry of Solid Surfaces, Collaborative Innovation Center of Chemistry for Energy Materials, College of Chemistry and Chemical Engineering, Xiamen University, Xiamen, 361005, China

ARTICLE INFO

Article history:

Received 1 September 2016
Received in revised form 19 January 2017
Accepted 19 January 2017
Available online 28 January 2017

Keywords:

Co_3O_4
Anion exchange
 Co_9S_8
Anode
Lithium-ion battery

ABSTRACT

Micro/nanostructured Co_9S_8 cubes and spheres ($\text{S-Co}_9\text{S}_8$) were successfully prepared with Co_3O_4 as templates via the vapor-based anion exchange reaction. The morphology and structure of both materials were characterized by SEM and XRD. Co_9S_8 microcubes and microspheres were composed of nanoparticles, inheriting the micro/nanostructure of Co_3O_4 precursors. Tested in lithium ion batteries, $\text{C-Co}_9\text{S}_8$ and $\text{S-Co}_9\text{S}_8$ anodes exhibited high specific capacities, excellent cycle stability ($\text{C-Co}_9\text{S}_8$: 369 mAh g^{-1} , $\text{S-Co}_9\text{S}_8$: 370 mAh g^{-1} over 300 cycles at 1C) and high rate performances ($\text{C-Co}_9\text{S}_8$: 450 mAh g^{-1} , $\text{S-Co}_9\text{S}_8$: $\sim 430 \text{ mAh g}^{-1}$ at 5C).

© 2017 Elsevier Ltd. All rights reserved.

1. Introduction

In modern society, lithium-ion batteries (LIBs) have been widely applied in electric vehicles and electronic devices owing to many advantages such as high energy, convenience, long cycle life, etc. [1–3]. However, the traditional graphitic anode has impeded further development of LIB due to its relative low specific capacity and electroplating of lithium, dissatisfying with the demand of next-generation energy storage systems [4,5]. $\text{Li}_4\text{Ti}_5\text{O}_{12}$ is a commercial material used as the anode with a relatively high charge/discharge plateaus ($\sim 1.7 \text{ V}$) to avoid formation of hazardous lithium dendrite and high structure stability to promise good cycling performance. Although such kind of material has advantages above, it has a low specific capacity (175 mAh g^{-1}) and specific energy (266 Wh kg^{-1}), which could not meet the requirement of high energy density batteries [6,7]. To meet the increasing demand of high density energy batteries, considerable effort has been focused on exploring new materials, among which metal sulfides have been broadly investigated as promising anode materials because of the high specific capacity and high rate performance [8–10]. In particular, cobalt sulfides with different stoichiometries have been widely studied as anodes since they exhibit high theoretical specific capacities (Co_9S_8 : 545 mAh g^{-1} ,

CoS : 589 mAh g^{-1} , Co_3S_4 : 702 mAh g^{-1}) and high electronic conductivity [11–13].

To obtain cobalt sulfides, numerous efforts have been made including synthesis of nano-sized material. For example, Zhou et al. synthesized Co_9S_8 hollow nanospheres with the reversible capacity of 896 mAh g^{-1} over 800 cycles at 2 A g^{-1} [14]. Wang et al. prepared graphene-wrapped CoS nanoparticles, delivering 749 mAh g^{-1} in 40 cycles at 0.1C [15]. Basically, the nano-sized material has lots of virtues: (1) The reduced particle size could shorten lithium insertion/removal pathway; (2) The larger specific surface area could insure a high contact with electrolytes to enhance reaction rates. However, the nano-sized material also possesses its disadvantages: (1) The nanoparticle may readily aggregate during long term cycling; (2) Low tap density would reduce the volumetric energy density of electrode [16]. To overcome these problems, attempts have been made to obtain micro-sized cobalt sulfides. Chen et al. synthesized porous CoS /carbon polyhedral structure exhibiting reversible capacity of 1668 mAh g^{-1} in 100 cycles [11]. Wang et al. synthesized cobalt sulfide embedded within nitrogen-doped carbon nanosheets ($\text{Co}_9\text{S}_8/\text{Co}_{1-x}\text{S@NC}$) composite, exhibiting excellent reversible capacity (1230 mAh g^{-1} over 110 cycles) and rate capability (813 mAh g^{-1} at 2000 mA g^{-1}) [17]. Metal-organic-framework derived and nanotubes supported Co_9S_8 /carbon composites are proposed to apply in LIBs, exhibiting desirable electrochemical performances [18,19]. Micro-sized cobalt sulfide particles were obtained for lithium ion batteries by Zhang et al. [20] Although the micro-sized materials own higher tap density, the electrochemical

* Corresponding authors. Tel.: +86 05922186935; fax: +86 05922186935.

E-mail addresses: wangjing2015@xmu.edu.cn (J. Wang), jbzhao@xmu.edu.cn (J.B. Zhao).

reaction rate is also reduced because of lower specific surface area. Therefore, a compromised strategy should be put forward. Recently, micro/nanostructured materials have gained much attention. The unique structure inherits both advantages of micro-sized material with high tap density and nano-sized material possessing enhanced specific surface area [21–23]. Synthesis of micro/nanostructured cobalt sulfides may be a probable way to obtain electrode materials for high performance energy storage systems.

In our work, micro/nanostructured Co_9S_8 microcubes and microspheres have been successfully prepared with the micro/nanostructured Co_3O_4 as the templates via vapor-based anion exchange method. Both Co_9S_8 microcubes and microspheres are composed of nanoparticles. Fabricated as anodes, they are tested in lithium ion batteries and exhibit high specific capacity, stable cycling stability and excellent rate capabilities.

2. Experimental Section

2.1. Material Synthesis

Co_3O_4 microcube and microsphere were firstly prepared by previously reported modified hydrothermal method [24–26]. All raw materials are purchased from Sinopharm Chemical Reagent Corporation without further treatment.

Co_3O_4 microcube (C- Co_3O_4): 1.8 g $\text{Co}(\text{CH}_3\text{COO})_2 \cdot 4\text{H}_2\text{O}$, 1.4 g triethanolamine (TEA), 2.1 g urea were dissolved in 70 mL deionized water followed by magnetic stirring, which was transferred to 100 mL Teflon-lined stainless steel autoclave. The autoclave was heated at 160 °C for 12 h to obtain precursors, which were washed by deionized water and ethanol for several times. The dried product was calcined in a muffle furnace at 600 °C for 10 h with a heating rate of 10 °C min^{-1} to obtain Co_3O_4 .

Co_3O_4 microsphere (S- Co_3O_4): 1.0 g $\text{CoCl}_2 \cdot 6\text{H}_2\text{O}$ and 2.0 g urea were dissolved in a mixed solution of glycerol (60 mL) and deionized water (20 mL). After stirred to transparent, the mixture was transferred to 100 mL Teflon-lined stainless steel autoclave, which was kept at 120 °C for 12 h. The product was washed by deionized water and ethanol followed by drying. The dried product was then calcined at 600 °C for 10 h in a muffle furnace with a heating rate of 10 °C min^{-1} .

Co_9S_8 microcube (C- Co_9S_8) and microsphere (S- Co_9S_8): 1.0 g as-prepared Co_3O_4 microcube (microsphere) and 2.0 g thiourea were placed in two different porcelain boats, one filled with Co_3O_4 was located in the middle of the quartz tube and the other was placed

near the inlet of the gas. The boats were heated at 350 °C for 6 h in the presence of 5% H_2/Ar gas mixture.

2.2. Structure Characterization

Crystal structures were characterized by X-ray diffraction (XRD, Rigagu/mini Flex 600) with a $\text{Cu K}\alpha$ radiation from 10° to 90° with scanning step of 2° min^{-1} . The operating voltage and current were 40 kV and 15 mA, respectively. Morphologies and elemental mapping were investigated with field emission scanning electron microscopy (SEM, Hitachi S-4800).

2.3. Electrochemical Measurement

The working electrodes were fabricated by casting the slurry, mixing 70 wt% of Co_9S_8 as active material, 15 wt% of acetylene black as the conductive agent and 15 wt% polyvinylidene difluoride (PVDF) as the binder in N-methyl-2-pyrrolidinone (NMP) onto the copper foil. The electrodes were dried at 60 °C for 12 h under vacuum. The mass loading of active material ranges from 1.2 mg cm^{-2} to 1.6 mg cm^{-2} . 2016-type coin cells were assembled in an argon-filled glove box with the lithium foil as the counter electrode and Celgard 2400 as the separator. The electrolyte is 1 M bis (trifluoromethanesulfonyl)imide lithium salt (LiTFSI, J&K Chemical) dissolved in 1, 3-dioxolane and dimethyl ether (DOL/DME in the 1:1 volume ratio, both purchased from Aladdin). Galvanostatic cycling was performed on the Neware battery program-control system at different rates from 1.0 V to 3.0 V versus Li^+/Li . Cyclic voltammetry (CV) tests of the first three cycles were conducted on the CHI 1030C electrochemical workstation with a scan rate of 0.2 mV s^{-1} from 1.0 V to 3.0 V. CV tests with different scan rates ranging from 0.2 mV s^{-1} to 2.0 mV s^{-1} were performed on the Metrohm Autolab PGSTAT 302N electrochemical workstation after 10 cycles in a fully charged state (3.0 V). The electrochemical impedance spectra (EIS) were measured (fully charged at 3.0 V at 1C) in different cycles in the frequency of 10⁻¹ Hz to 10⁵ Hz on the Solartron Modulab 1287/1260. The cycle performance was tested at 1C (1 C = 545 mA g^{-1}) and 2C.

3. Results and Discussion

The synthesis scheme is shown in Fig. 1. The reactions were carried out in the furnace and the detail is shown in experimental section. The micro/nanostructured Co_3O_4 precursors are chosen because the micro-meter size ensures a high volumetric specific

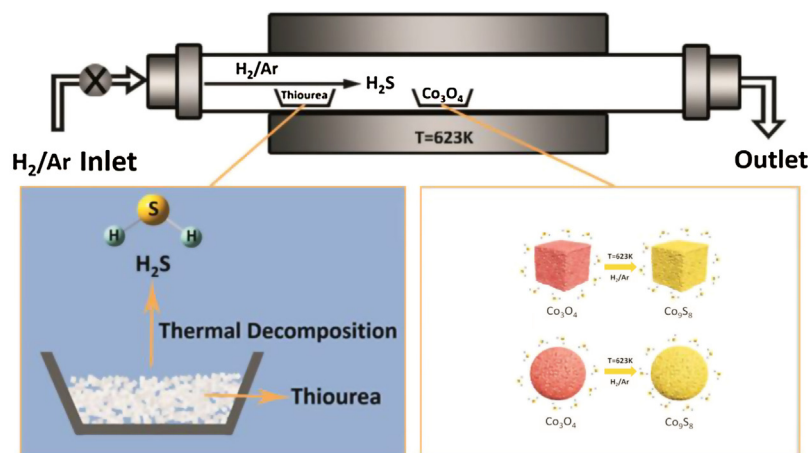


Fig. 1. Sketch map of synthesis route.

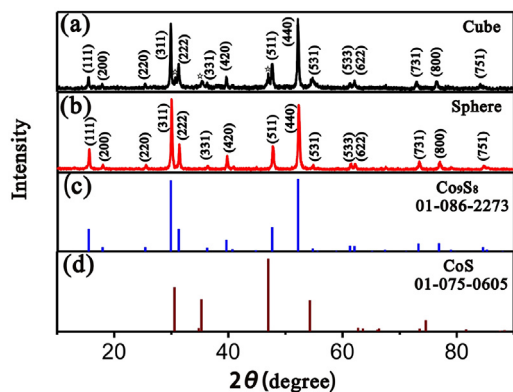


Fig. 2. XRD patterns of (a) Co₉S₈ microcubes (C-Co₉S₈), (b) Co₉S₈ microspheres (S-Co₉S₈) and (c, d) corresponding standard material cards.

capacity and the mesoporous nanostructure guarantees high specific surface area for increasing contact area with electrolytes. The vapor-based anion exchange reaction is preferred since it barely induces destruction to the precursors' structure, which is suitable for preparing micro-sized materials [11,12]. H₂S, as one of sulfur sources, is commonly used to transform oxides to sulfides [27]. Therefore, we employ as thiourea as the sulfur source, which

is thermally decomposed to form H₂S gas above 180 °C [28]. At 350 °C, the H₂S gas floated from the inlet to the outlet, Co₃O₄ precursors experienced the anion exchange process with H₂S and were transformed to Co₉S₈ with maintained particle sizes and morphologies.

The crystal phases of both micro/nanostructured Co₃O₄ materials were ascertained by XRD, as shown in Fig. S1. Diffraction patterns (Fig. S1a, S1b) of Co₃O₄ precursors match well with the standard one (Fig. S1c). After anion exchange, the peaks indexed to Co₃O₄ completely disappear. As seen from Fig. 2a, the XRD pattern is mainly ascribed to C-Co₉S₈ while weak peaks at 31.0°, 35.1° and 47.0° indicates a small quantity of CoS. The spherical one is completely transformed to S-Co₉S₈, whose peaks match well up with the Co₉S₈ standard card (Fig. 2b), illustrating that the transformation from Co₃O₄ to Co₉S₈ is complete.

Scanning electron microscopy images (Fig. 3a–c) show that the size of C-Co₃O₄ is about 10 μm. The microcube is composed of primary nanoparticles with the average size of 200 nm, whose surface is full of pores. After sulfidation, the morphology and particle size (Fig. 3d–f) are well maintained, while the primary nanoparticles' size becomes larger and the surface structure becomes more compact. The SEM images of S-Co₃O₄ are shown in Fig. 4a–c. The average diameter of S-Co₃O₄ is in the micro-size regime. Each particle is composed of primary nanoparticles with the size of ~100 nm, whose surface is also full of pores like the C-Co₃O₄. The SEM images (Fig. 4d–f) show that the morphology and

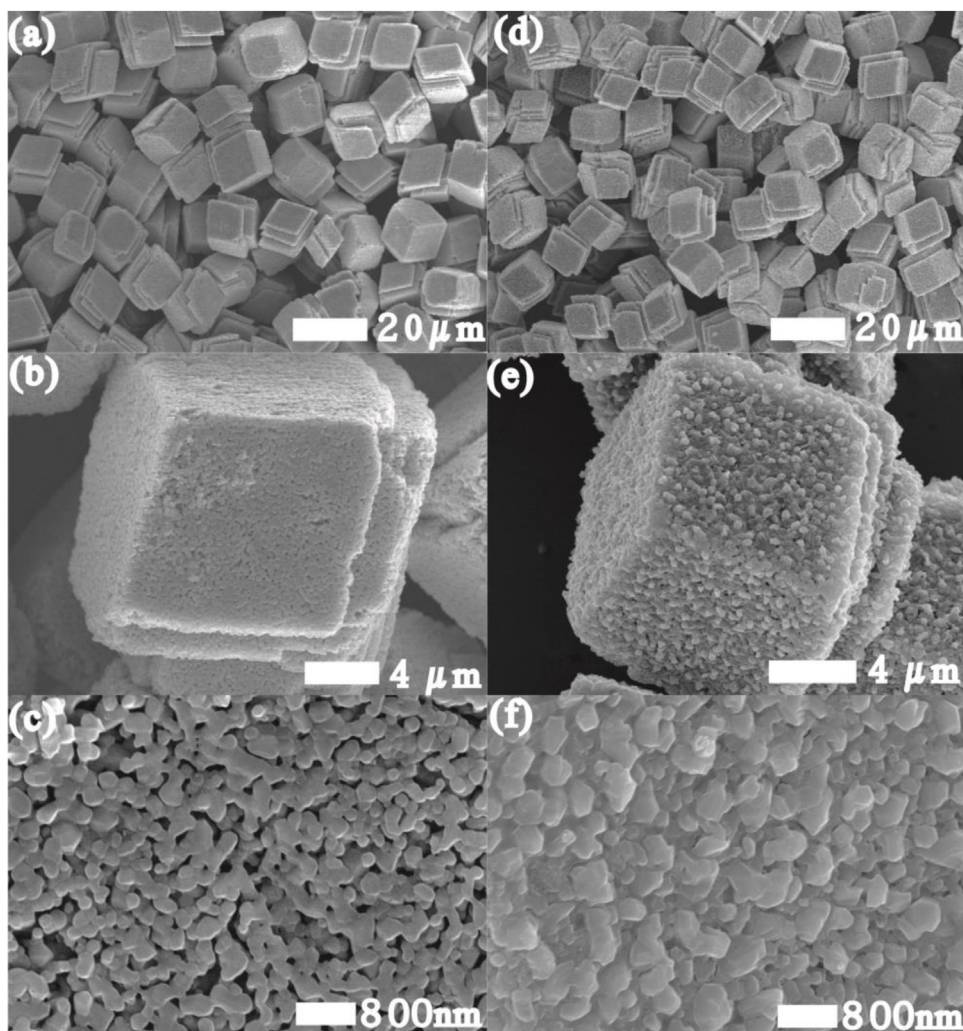


Fig. 3. SEM images of (a–c) Co₃O₄ and (d–f) C-Co₉S₈.

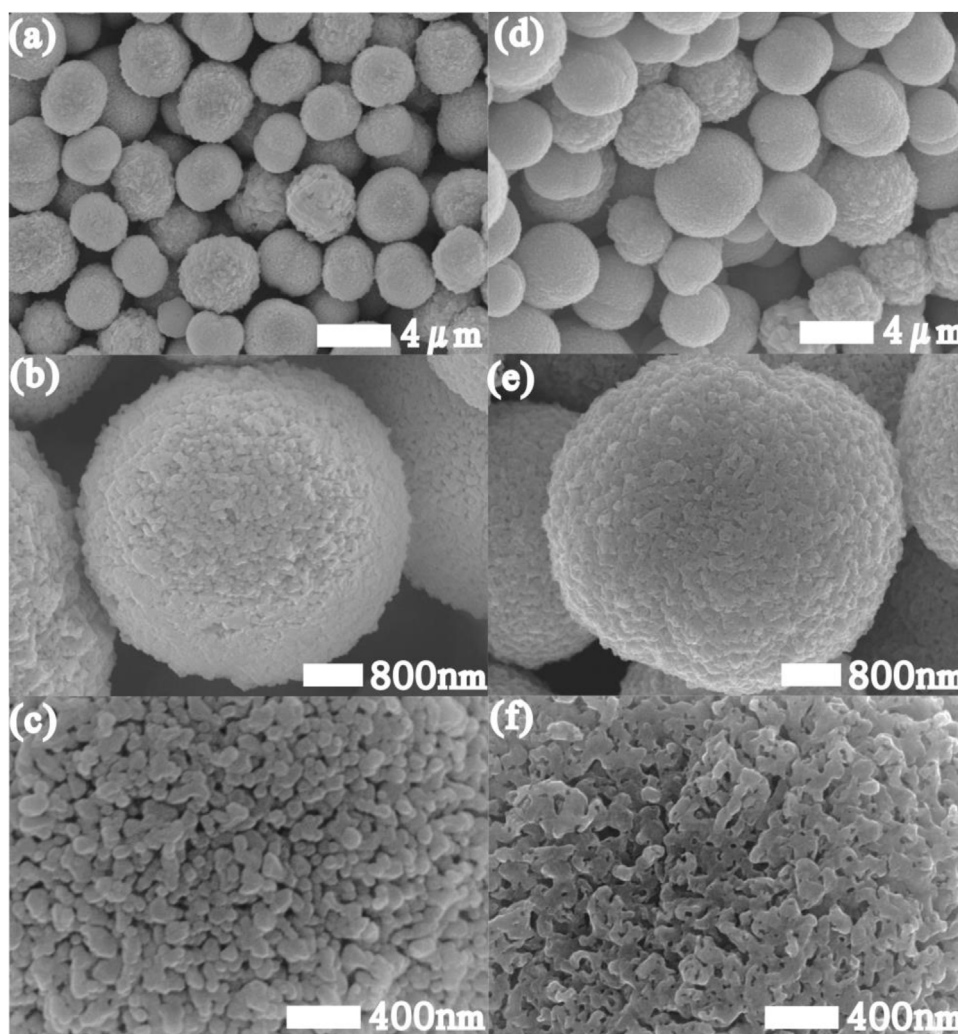


Fig. 4. SEM images of (a–c) Co_3O_4 and (d–f) $\text{S-Co}_9\text{S}_8$.

the surface of $\text{S-Co}_9\text{S}_8$ has no obvious change after anion exchange by sulfur. To know well with the elemental distribution of $\text{C-Co}_9\text{S}_8$ and $\text{S-Co}_9\text{S}_8$, elemental mapping analysis was applied as shown in Fig. 5. The mapping images confirm that element Co and S distribute homogeneously in both cases, which could be observed more clearly from the superposed images (Fig. 5g and h).

The electrochemical performances of $\text{C-Co}_9\text{S}_8$ and $\text{S-Co}_9\text{S}_8$ anodes were evaluated in 2016-type coin cells. The voltage between 1.0 V and 3.0 V is chosen in this work because, for cobalt sulfides, the discharge plateau corresponding to conversion reaction is above 1.0 V [29]. Besides, many unexpected side reactions including decomposition of electrolytes would take place when the cut-off voltage is below 0.7 V, leading to low initial coulombic efficiency [30,31]. The CV curves of the $\text{C-Co}_9\text{S}_8$ electrode are shown in Fig. 6a, a broad and strong cathodic peak at 1.05 V appears in the initial cycle, which is ascribed to the conversion reaction: $\text{Co}_9\text{S}_8 + 16\text{Li} \rightarrow 9\text{Co} + 8\text{Li}_2\text{S}$ [29,32]. Two anodic peaks at 1.98 V and 2.38 V are observed, indicating that the procedure of charge is a two-step process. Firstly, the discharge products are transformed to intermediates ($\text{Li}_x\text{Co}_9\text{S}_8$ or Co_xS_y) at the voltage of 1.98 V followed by oxidation of intermediates to Co_xS and Li, which is consistent with other works [32–35]. In the second scanning, a weak cathodic peak at 1.78 V related to the formation of intermediates evolves and the strong cathodic peak shifts to 1.24 V. The anodic peak at 2.02 V becomes sharper. In the 3rd scanning, the strong cathodic peak continues to positively shift, implying the

electrochemical polarization becomes smaller and the electrochemical reversibility becomes better. CV curves of the $\text{S-Co}_9\text{S}_8$ electrode shown in Fig. 6b are the same as the previous report [36], while a little different from those of $\text{C-Co}_9\text{S}_8$. The shape of redox peaks is different. The cathodic peak at 1.12 V ascribing to reduction of Co_9S_8 to Co and Li_2S is sharper. Besides, the redox peaks in $\text{S-Co}_9\text{S}_8$ are less than those of $\text{C-Co}_9\text{S}_8$. There's no cathodic peak ($\sim 1.8\text{V}$) and the anodic peak ($\sim 1.9\text{V}$) relating with the formation and decomposition of intermediates in the first three cycles. In subsequent cycles, both anodic and cathodic peaks positively shift, while the voltage gap between redox peaks becomes smaller, demonstrating the improvement in the electrochemical reversibility.

Fig. 6c and d display the charge-discharge curves of $\text{C-Co}_9\text{S}_8$ and $\text{S-Co}_9\text{S}_8$ anodes at 1C. For the $\text{C-Co}_9\text{S}_8$ electrode, two plateaus (around 1.4 V and 1.2 V) exist in the initial discharge process, which are consistent with the broad and strong anodic peaks in the 1st scanning of the CV measurement. There is a long plateau (around 1.8 V) and a sloped plateau (2.4 V) during the charge process. As discussed above, the plateau at 1.8 V corresponds to the formation of intermediates and the one at 2.4 V is ascribed to the continuing oxidation of intermediates to form Co_xS and Li. With cycling, the charge-discharge curves of $\text{C-Co}_9\text{S}_8$ have changed. In the 10th cycle, a pair of sloped plateau (around 1.75 V in discharge and around 2.2 V in charge) appears, which is related with the intermediates. For the $\text{S-Co}_9\text{S}_8$ electrode, the characteristic of

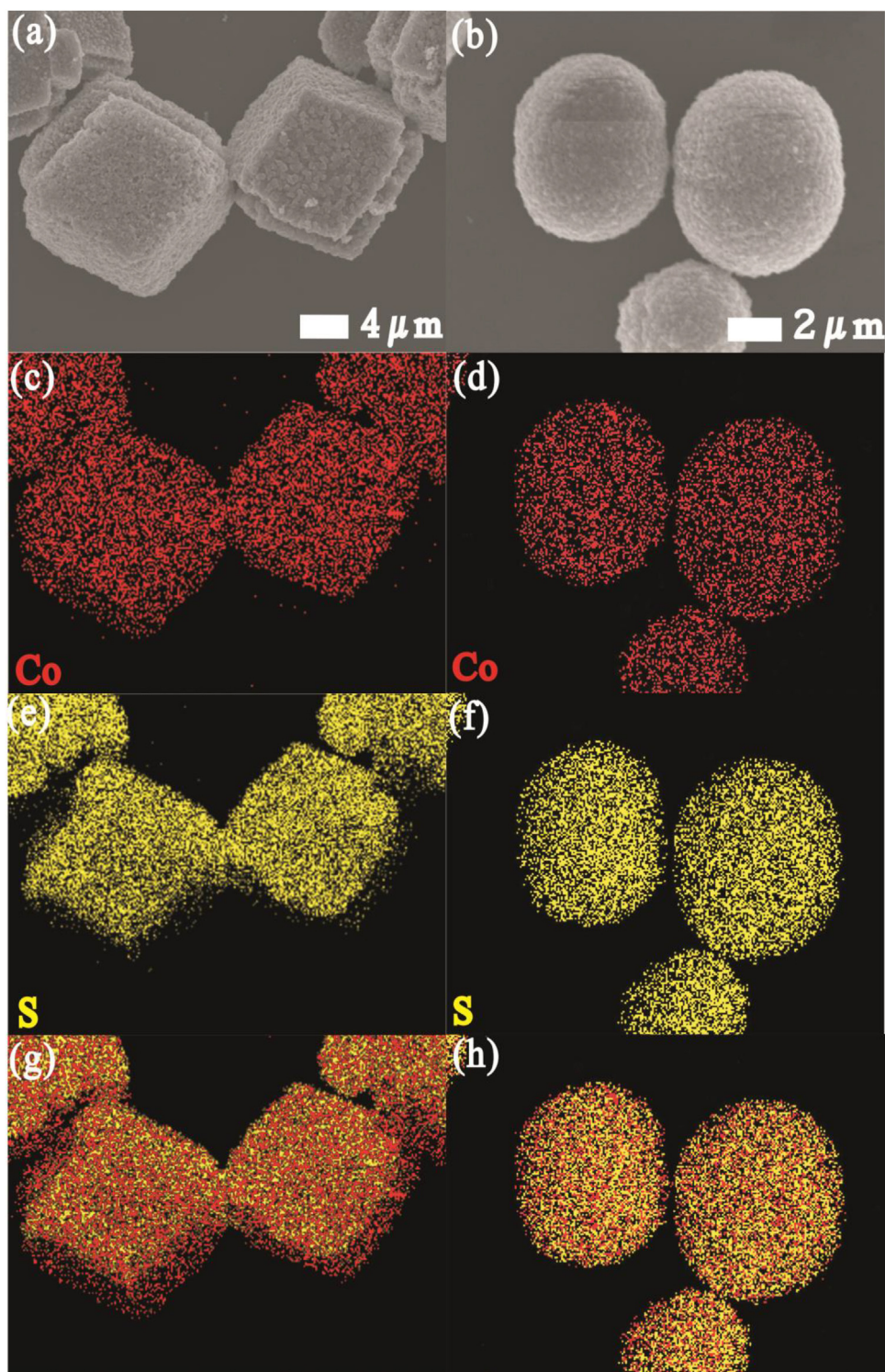


Fig. 5. SEM images of (a) C-Co₉S₈ and (b) S-Co₉S₈ and corresponding elemental mapping of (c, d) Co, (e, f) S, (g, h) superposed ones.

charge-discharge profiles corresponds with the CV curves in the first three cycles. However, the charge-discharge profile has changed after 10 cycles, which is similar with that of C-Co₉S₈, indicating the similar electrochemical behavior between two electrodes. The initial discharge capacities of C-Co₉S₈ and S-Co₉S₈ are 599 mAh g⁻¹ and 550 mAh g⁻¹, respectively. Since the theoretical capacity of Co₉S₈ is 545 mAh g⁻¹, the formation of intermediates is assumed to contribute to partial capacity leading to the

extra discharge capacity of C-Co₉S₈ as reported results [10,34,37]. There is no extra capacity in the initial discharge process of S-Co₉S₈ (corresponding with only a plateau).

Long term cycle experiments are performed at 1C (545 mAh g⁻¹) and 2C between 1.0 V and 3.0 V (vs. Li), as shown in Fig. 6e and f. For both electrodes, the cycle performance is fluctuating. In the first 30 cycles, the capacity drops severely, which may be caused by the irreversible structure transformation and side-reactions with

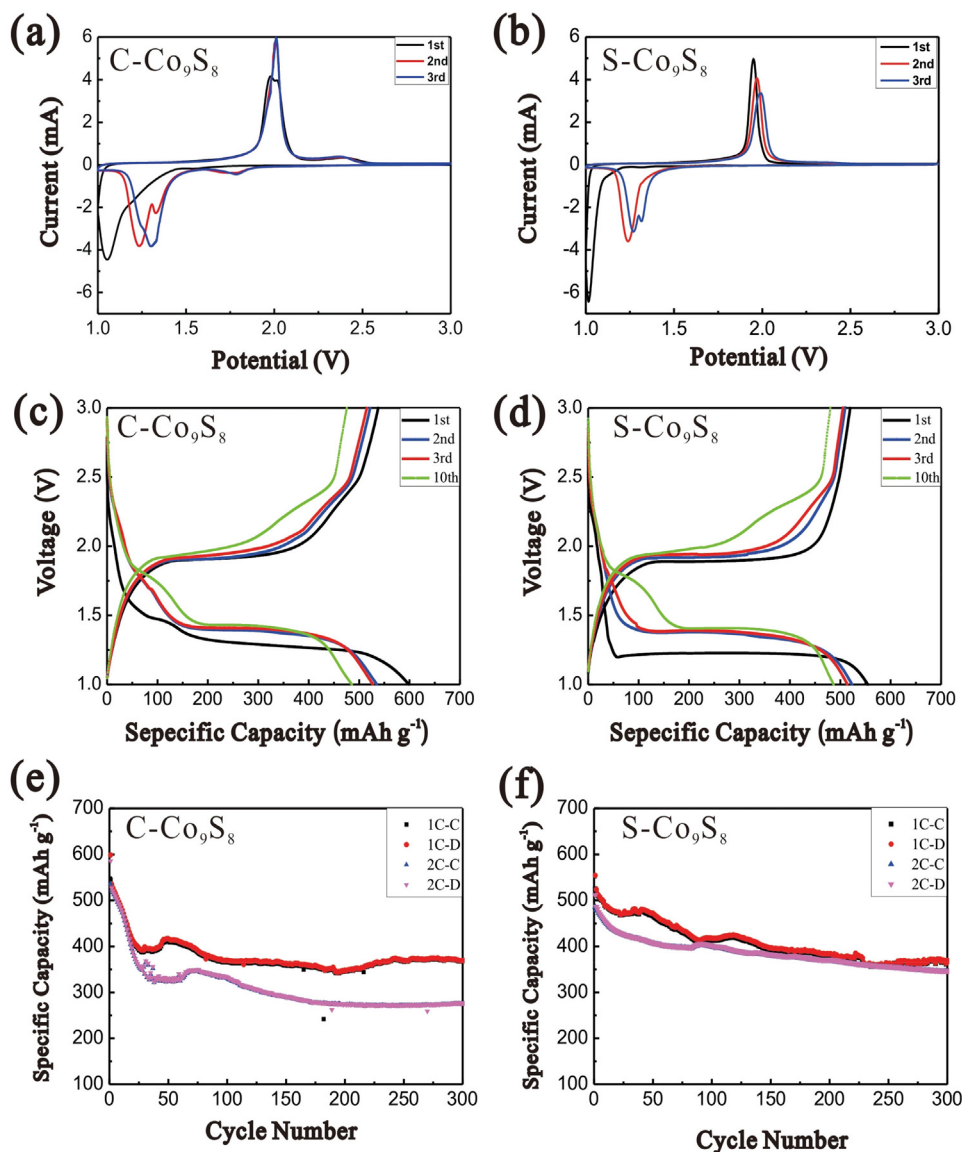


Fig. 6. Cyclic voltammetry profiles of the (a) C-Co₉S₈ and (b) S-Co₉S₈ electrodes at 0.2 mV s⁻¹ in the voltage range of 1.0–3.0 V. Charge-discharge curves of the (c) C-Co₉S₈ and (d) S-Co₉S₈ electrodes at 1C, cycle performances of (e) C-Co₉S₈ and (f) S-Co₉S₈ electrodes at 1C and 2C, respectively.

the electrolytes [12,14,15,38,39]. After 100 cycles, the cycling stability becomes better, which is similar with results reported by other group [39,40]. It is suspected to correlate with formation of stable interface and structure of active material, which needs further investigation. After 300 cycles, the C-Co₉S₈ electrode maintains at more than 370 mAh g⁻¹ and 277 mAh g⁻¹ and the S-Co₉S₈ electrode possesses around 369 mAh g⁻¹ and 347 mAh g⁻¹ at 1C and 2C, respectively. The decay rates are very low, 0.127% and 0.176% per circle for the C-Co₉S₈ electrode, and 0.109% and 0.107% per circle for the S-Co₉S₈ electrode, at 1C and 2C, respectively. It is noted that current density makes a larger difference in the cycle

performances of C-Co₉S₈, especially at 2C, which is supposed to be related with the particle size. As seen from SEM images (Figs. 3 and 4), the particle size of C-Co₉S₈ is about 10 μm, which is about two-fold larger than that of S-Co₉S₈. The larger particle size would lengthen the Li⁺ insertion pathway, which may affect the rate capability. To know more about the lithium ion diffusion in the material, the Randles-Sevik equation (1) (eqn 1) was applied [41]:

$$I_p = 0.4463n^{3/2}F^{3/2}CSR^{-1/2}T^{-1/2}D^{1/2}v^{1/2} \quad (1)$$

where I_p is the peak current, F is the Faraday constant, n is the charge transfer number, C is the concentration of Li⁺, S is the

Table 1
The discharge capacities in the 1st and 300th cycles and corresponding decay rates of C-Co₉S₈ and S-Co₉S₈ electrodes at 1C and 2C.

Rate	C-Co ₉ S ₈			S-Co ₉ S ₈		
	Discharge Capacity (mAh g ⁻¹)		Decay Rate (%)	Discharge Capacity (mAh g ⁻¹)		Decay Rate (%)
	1st cycle	300th cycle		1st cycle	300th cycle	
1C	599	370	0.127	550	369	0.109
2C	586	277	0.176	512	347	0.107

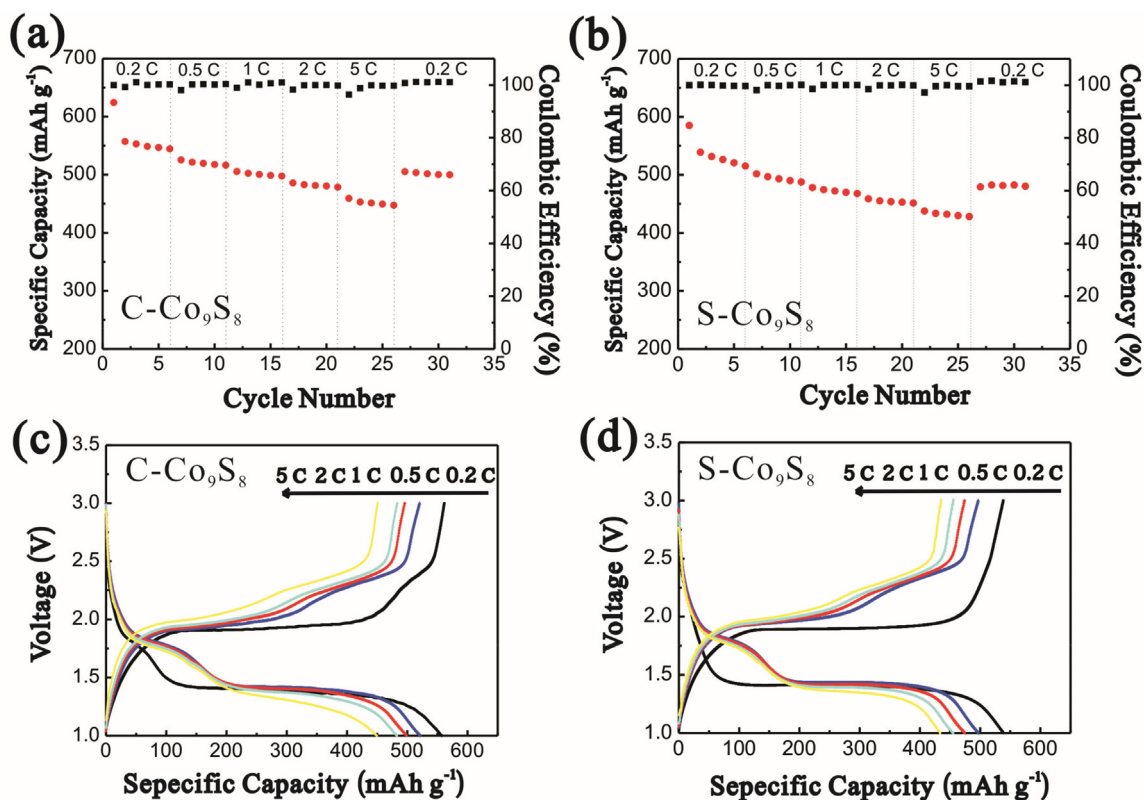


Fig. 7. Rate capability and corresponding charge-discharge curves of the (a, c) C-Co₉S₈ and (b, d) S-Co₉S₈ electrodes.

electrode surface area, R is the gas constant, T is the temperature, D is the apparent chemical diffusion coefficient of Li^+ , ν is the scan rate. In brief, the formula could be simplified as equation (2) (eqn 2):

$$I_p = K\nu^{1/2} \quad (2)$$

where K represents all factors containing the apparent chemical diffusion coefficient D and is also the slope of the equation. From eqn 1, it can be known that the absolute value of K is proportional to D . To obtain the value of K , different CV scan rates were applied and corresponding curves are shown in Fig. S2a, 2b. The redox peak current increases with increasing scan rates and the redox peak current scales linearly with the square root of the scan rate (Fig. S2c). The slopes (K) of oxidation fitting lines are 7.99 and 3.61 $\text{cm}^2 \text{s}^{-1}$ and the slopes of reduction fitting lines are -9.41 and $-4.83 \text{ cm}^2 \text{s}^{-1}$ for S-Co₉S₈ and C-Co₉S₈, respectively. The K for S-Co₉S₈ is twice as much as that of C-Co₉S₈, which indicates the faster lithium ion diffusion in S-Co₉S₈. Besides, the structure stability of spherical shape may make a difference in the cycle performance [42,43]. All data related with discharge capacity as well as the decay rates in both cases in the 1st and 300th cycle is summed up in Table 1. Although the cycling performance of C-Co₉S₈ is inferior to that of S-Co₉S₈, it is difficult to draw a conclusion that whether cubes or spheres are good in this work and the reasons are as follow: 1) the particle sizes of synthetic cubes and spheres are not the same, leading to different Li^+ insertion pathway; 2) the crystallinity of material can make a difference in the electrochemical performances, though prepared at the same temperature, the crystallinity of cubes and spheres in this work is different. 3) the interface property is also a key factor influencing the electrochemical performances. Therefore, a more well-designed experiment and efforts are needed to verify this speculation.

Fig. 7a and b display the rate performances of C-Co₉S₈ and S-Co₉S₈ electrodes when the C rate is gradually increased from 0.2C

to 5C over 30 cycles. For the C-Co₉S₈ electrode, capacities of 547, 520, 498, 480 and 450 mAh g^{-1} can be achieved at 0.2, 0.5, 1, 2 and 5C, respectively, which shows no dramatic capacity fading. When the rate is turned back to 0.2C, about 92.0% of the capacity is recovered and no obvious capacity loss is observed after 30 cycles. For the S-Co₉S₈ electrode, capacities of 532, 492, 472, 455 and 432 mAh g^{-1} can be gained at 0.2, 0.5, 1, 2 and 5C. 90.6% of capacity can be regained when the rate is turned back. Fig. 7c and d show the corresponding charge-discharge curves, the gaps between charge and discharge plateaus become larger due to the polarization in both charge and discharge processes for two cases. Similar with other works, the micro/nanostructured materials show superior electrochemical performances [25,26].

To gain information about the kinetics of electrodes, electrochemical impedance spectra (EIS) were conducted before cycling and after 30 cycles as shown in Fig. 8. In order to fitting the impedance data well, the equivalent circuit diagram is used (Fig. 8c), where R_s is the internal resistance of tested batteries, R_{er} and CPE are related with the cell's reaction resistance, W_o represents the Warburg impedance relating to the Li^+ diffusion process [44,45]. As shown in Fig. 8a and b, for both cases, a relatively large depressed semicircle exists before cycling which dramatically shrinks after 20 cycles. Table 2 shows the EIS parameters of both electrodes, the R_{er} greatly reduces from 58.5 Ω to 1.85 Ω and from 97.8 Ω to 3.30 Ω after 40 cycles in the case of C-Co₉S₈ and S-Co₉S₈ anodes. The dramatic decline of R_{er} means electrochemically activation of anodes, whose activation process is supposed to be related with the infiltration of lithium salt and electrolytes into micro-size particle. To further analyze electrochemical behavior of long term cycling, EIS was implemented after 300 cycles and corresponding equivalent circuit is shown in Fig. S3. Obviously, the curves are composed of two depressed semi-circles and a slope line, which means the R_{er} is divided into two part, the ohmic surface layer resistance (R_{s1}) at the

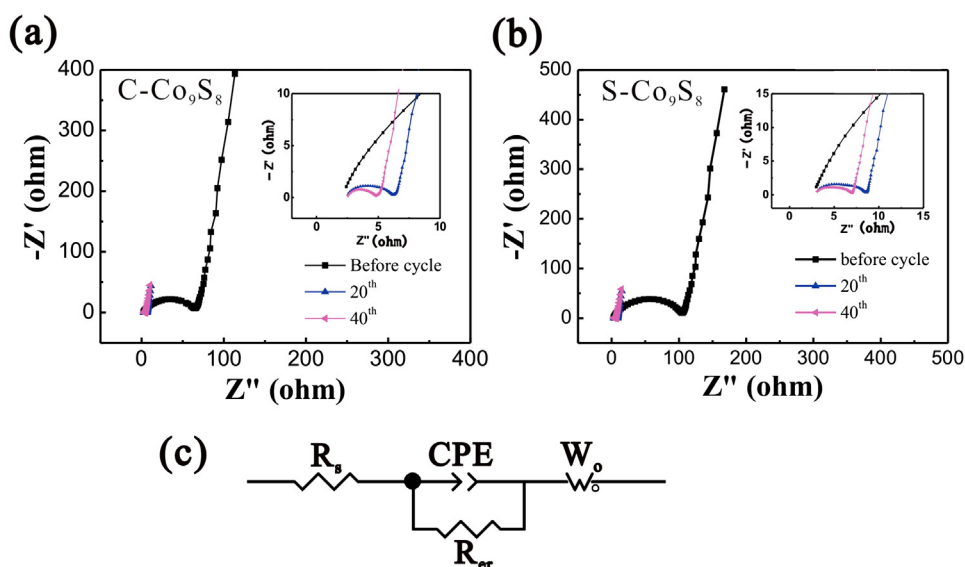


Fig. 8. Electrochemical impedance spectroscopy (EIS) curves of the (a) C-Co₉S₈ and (b) S-Co₉S₈ electrodes (charged at 3.0 V) in different cycles over the frequency from 0.1 Hz to 1 MHz, and (c) the equivalent circuit.

Table 2
Impedance parameters of C-Co₉S₈ and S-Co₉S₈ electrodes.

	C-Co ₉ S ₈				S-Co ₉ S ₈			
	R _s (Ω)	Error (%)	R _{er} (Ω)	Error (%)	R _s (Ω)	Error (%)	R _{er} (Ω)	Error (%)
Before cycle	2.15	1.71	58.5	2.79	2.68	0.872	97.8	0.973
20th	2.63	0.895	3.32	1.10	3.18	0.964	5.16	3.60
40th	2.71	0.937	1.85	1.62	3.09	0.867	3.30	1.65

high frequency and the charge transfer impedance (R_{ct}) at the middle frequency [44]. From the EIS parameters shown in Table S1, it can be seen that there is no great change for R_s , whereas the R_{s1} and R_{ct} increase remarkably, the R_{ct} of S-Co₉S₈ is 341 Ω, which is larger than that of C-Co₉S₈, indicating greater difficulty of transferring electron between the active material and electrolytes for S-Co₉S₈, which may explain the more deteriorative long term (>200 cycles) cycle performance for S-Co₉S₈ of electrodes.

5. Conclusion

In conclusion, Co₉S₈ microcube and microsphere were successfully prepared via vapor-based anion exchange reactions with Co₃O₄ as precursors. Fabricated as electrodes, both materials were measured in varieties of electrochemical performance tests, which show outstanding cycle performances and rate capability. After 300 cycles, the C-Co₉S₈ electrode releases more than 370 mAh g⁻¹ and 277 mAh g⁻¹ and the S-Co₉S₈ electrode possesses around 369 mAh g⁻¹ and 347 mAh g⁻¹ at 1C and 2C, respectively. At the high rate of 5C, the C-Co₉S₈ and S-Co₉S₈ anodes can gain more than capacity of 430 mAh g⁻¹. As new classes of anode materials, they can be regarded as a kind of hopeful electrode candidate for the high performance energy storage system.

Acknowledgement

We gratefully acknowledge the financial support of National Natural Science Foundation of China (Grant Nos. 21273185 and

21321062). The authors also wish to express gratitude to Dr. Dong Sun and Dr. Weidong He.

Appendix A. Supplementary data

Supplementary data associated with this article can be found, in the online version, at <http://dx.doi.org/10.1016/j.electacta.2017.01.122>.

References

- [1] J.W. Choi, D. Aurbach, Promise and reality of post-lithium-ion batteries with high energy densities, *Nat. Rev. Mater* 1 (2016) 16013.
- [2] J.B. Goodenough, Electrochemical energy storage in a sustainable modern society, *Energy Environ. Sci.* 7 (2014) 14–18.
- [3] Y. Wang, B. Liu, Q. Li, S. Cartmell, S. Ferrara, Z.D. Deng, J. Xiao, Lithium and lithium ion batteries for applications in microelectronic devices: A review, *J. Power Sources* 286 (2015) 330–345.
- [4] J.B. Goodenough, Y. Kim, Challenges for Rechargeable Li Batteries†, *Chem. Mater.* 22 (2010) 587–603.
- [5] P.G. Bruce, B. Scrosati, J.M. Tarascon, Nanomaterials for rechargeable lithium batteries, *Angew. Chem. Int. Ed.* 47 (2008) 2930–2946.
- [6] G.-N. Zhu, Y.-G. Wang, Y.-Y. Xia, Ti-based compounds as anode materials for Li-ion batteries, *Energy Environ. Sci.* 5 (2012) 6652.
- [7] X. Li, H.-c. Lin, W.-j. Cui, Q. Xiao, J.-b. Zhao, Fast Solution-Combustion Synthesis of Nitrogen-Modified Li₄Ti₅O₁₂ Nanomaterials with Improved Electrochemical Performance, *ACS Appl. Mater. Interfaces* 6 (2014) 7895–7901.
- [8] X. Xu, W. Liu, Y. Kim, J. Cho, Nanostructured transition metal sulfides for lithium ion batteries: Progress and challenges, *Nano Today* 9 (2014) 604–630.
- [9] X. Wang, Y. Wang, X. Li, B. Liu, J. Zhao, A facile synthesis of copper sulfides composite with lithium-storage properties, *J. Power Sources* 281 (2015) 185–191.
- [10] Y. Wang, X. Li, Y. Zhang, X. He, J. Zhao, Ether based electrolyte improves the performance of CuFeS₂ spike-like nanorods as a novel anode for lithium storage, *Electrochim. Acta* 158 (2015) 368–373.

- [11] R. Wu, D.P. Wang, X. Rui, B. Liu, K. Zhou, A.W. Law, Q. Yan, J. Wei, Z. Chen, In-Situ Formation of Hollow Hybrids Composed of Cobalt Sulfides Embedded within Porous Carbon Polyhedra/Carbon Nanotubes for High-Performance Lithium-Ion Batteries, *Adv. Mater.* 27 (2015) 3038–3044.
- [12] J.H. Kim, J.-H. Lee, Y.C. Kang, Electrochemical properties of cobalt sulfide-carbon composite powders prepared by simple sulfidation process of spray-dried precursor powders, *Electrochim. Acta* 137 (2014) 336–343.
- [13] G. Huang, T. Chen, Z. Wang, K. Chang, W. Chen, Synthesis and electrochemical performances of cobalt sulfides/graphene nanocomposite as anode material of Li-ion battery, *J. Power Sources* 235 (2013) 122–128.
- [14] Y. Zhou, D. Yan, H. Xu, J. Feng, X. Jiang, J. Yue, J. Yang, Y. Qian, Hollow nanospheres of mesoporous Co_3S_8 as a high-capacity and long-life anode for advanced lithium ion batteries, *Nano Energy* 12 (2015) 528–537.
- [15] H. Wang, S. Lu, Y. Chen, L. Han, J. Zhou, X. Wu, W. Qin, Graphene/ Co_3S_8 nanocomposite paper as a binder-free and free-standing anode for lithium-ion batteries, *J. Mater. Chem. A* 3 (2015) 23677–23683.
- [16] P.G. Bruce, B. Scrosati, J.M. Tarascon, Nanomaterials for rechargeable lithium batteries, *Angew. Chem. Int. Ed.* 47 (2008) 2930–2946.
- [17] J. Wang, F. Bai, X. Chen, Y. Lu, W. Yang, Intercalated $\text{Co}(\text{OH})_2$ -derived flower-like hybrids composed of cobalt sulfide nanoparticles partially embedded in nitrogen-doped carbon nanosheets with superior lithium storage, *J. Mater. Chem. A* (2017) in press.
- [18] J. Liu, C. Wu, D. Xiao, P. Kopold, L. Gu, P.A. van Aken, J. Maier, Y. Yu, MOF-Derived Hollow Co_9S_8 Nanoparticles Embedded in Graphitic Carbon Nanocages with Superior Li-Ion Storage, *Small* 12 (2016) 2354–2364.
- [19] Y. Zhou, D. Yan, H. Xu, S. Liu, J. Yang, Y. Qian, Multiwalled carbon nanotube@ $\text{a-C@Co}_3\text{S}_8$ nanocomposites: a high-capacity and long-life anode material for advanced lithium ion batteries, *Nanoscale* 7 (2015) 3520–3525.
- [20] Y. Wang, J. Wu, Y. Tang, X. Lu, C. Yang, M. Qin, F. Huang, X. Li, X. Zhang, Phase-controlled synthesis of cobalt sulfides for lithium ion batteries, *ACS Appl. Mater. Interfaces* 4 (2012) 4246–4250.
- [21] X. Lai, J.E. Halpert, D. Wang, Recent advances in micro-/nano-structured hollow spheres for energy applications: From simple to complex systems, *Energy Environ. Sci.* 5 (2012) 5604–5618.
- [22] X.S. Zhang, F.Y. Zhu, M.D. Han, X.M. Sun, X.H. Peng, H.X. Zhang, Self-cleaning poly(dimethylsiloxane) film with functional micro/nano hierarchical structures, *Langmuir* 29 (2013) 10769–10775.
- [23] X. Wu, P. Jiang, W. Cai, X.D. Bai, P. Gao, S.S. Xie, Hierarchical ZnO Micro-/Nano-Structure Film, *Adv. Eng. Mater.* 10 (2008) 476–481.
- [24] B. Wu, J. Wang, J. Li, W. Lin, H. Hu, F. Wang, S. Zhao, C. Gan, J. Zhao, Morphology controllable synthesis and electrochemical performance of LiCoO_2 for lithium-ion batteries, *Electrochim. Acta* 209 (2016) 315–322.
- [25] G. Huang, S. Xu, S. Lu, L. Li, H. Sun, Micro-/nanostructured Co_3O_4 anode with enhanced rate capability for lithium-ion batteries, *ACS Appl. Mater. Interfaces* 6 (2014) 7236–7243.
- [26] S.-W. Bian, L. Zhu, Template-free synthesis of mesoporous Co_3O_4 with controlled morphologies for lithium ion batteries, *RSC Advances* 3 (2013) 4212–4215.
- [27] Y.N. Ko, S.H. Choi, S.B. Park, Y.C. Kang, Preparation of Yolk-Shell and Filled Co_3S_8 Microspheres and Comparison of their Electrochemical Properties, *Chem. Asian J.* 9 (2014) 572–576.
- [28] V.P. Timchenko, A.L. Novozhilov, O.A. Slepysheva, Kinetics of Thermal Decomposition of Thiourea, *Russian J. General Chem.* 74 (2004) 1046–1050.
- [29] Y. Kim, J.B. Goodenough, Lithium Insertion into Transition-Metal Monosulfides: Tuning the Position of the Metal 4s Band, *J. Phys. Chem. C* 112 (2008) 15060–15064.
- [30] A. Ponrouch, P.-L. Taberna, P. Simon, M.R. Palacín, On the origin of the extra capacity at low potential in materials for Li batteries reacting through conversion reaction, *Electrochim. Acta* 61 (2012) 13–18.
- [31] Y.F. Zhukovskii, P. Balaya, E.A. Kotomin, J. Maier, Evidence for Interfacial-Synthesis Anomaly in Nanocomposites for Lithium Batteries from First-Principles Simulations, *Phys. Rev. Lett.* 96 (2006).
- [32] J.L. Gómez-Cámer, F. Martín, J. Morales, L. Sánchez, Precipitation of CoS vs Ceramic Synthesis for Improved Performance in Lithium Cells, *J. Electrochem. Soc.* 155 (2008) A189–A195.
- [33] J. Wang, S.H. Ng, G.X. Wang, J. Chen, L. Zhao, Y. Chen, H.K. Liu, Synthesis and characterization of nanosize cobalt sulfide for rechargeable lithium batteries, *J. Power Sources* 159 (2006) 287–290.
- [34] S.S. Zhang, D.T. Tran, Electrochemical verification of the redox mechanism of FeS_2 in a rechargeable lithium battery, *Electrochim. Acta* 176 (2015) 784–789.
- [35] Z.X. Huang, Y. Wang, J.L. Wong, W.H. Shi, H.Y. Yang, Synthesis of self-assembled cobalt sulphide coated carbon nanotube and its superior electrochemical performance as anodes for Li-ion batteries, *Electrochim. Acta* 167 (2015) 388–395.
- [36] Y. Chen, J.-M. Tarascon, C. Guery, CV-Exploring sulfur solubility in ionic liquids for the electrodeposition of sulfide films with their electrochemical reactivity toward lithium, *Electrochim. Acta* 99 (2013) 46–53.
- [37] S.S. Zhang, The redox mechanism of FeS_2 in non-aqueous electrolytes for lithium and sodium batteries, *J. Mater. Chem. A* 3 (2015) 7689–7694.
- [38] Q. Zhou, L. Liu, Z.F. Huang, L.G. Yi, X.Y. Wang, G.Z. Cao, $\text{EIS-Co}_3\text{S}_4$ @polyaniline nanotubes as high-performance anode materials for sodium ion batteries, *J. Mater. Chem. A* 4 (2016) 5505–5516.
- [39] Y.X. Zhou, H.B. Yao, Y. Wang, H.L. Liu, M.R. Gao, P.K. Shen, S.H. Yu, Hierarchical hollow Co_9S_8 microspheres: solvothermal synthesis, magnetic, electrochemical, and electrocatalytic properties, *Chemistry* 16 (2010) 12000–12007.
- [40] Q. Wang, L. Jiao, Y. Han, H. Du, W. Peng, Q. Huan, D. Song, Y. Si, Y. Wang, H. Yuan, CoS_2 Hollow Spheres: Fabrication and Their Application in Lithium-Ion Batteries, *J. Phys. Chem. C* 115 (2011) 8300–8304.
- [41] Y. You, H.R. Yao, S. Xin, Y.X. Yin, T.T. Zuo, C.P. Yang, Y.G. Guo, Y. Cui, L.J. Wan, J.B. Goodenough, GITT-CV-EIS-Subzero-Temperature Cathode for a Sodium-Ion Battery, *Adv. Mater.* 28 (2016) 7243–7248.
- [42] J. Ying, C. Jiang, C. Wan, Preparation and characterization of high-density spherical LiCoO_2 cathode material for lithium ion batteries, *J. Power Sources* 129 (2004) 264–269.
- [43] F. Wang, Z. Wen, C. Shen, K. Rui, X. Wu, C. Chen, Open mesoporous spherical shell structured Co_3O_4 with highly efficient catalytic performance in Li-O_2 batteries, *J. Mater. Chem. A* 3 (2015) 7600–7606.
- [44] S.S. Zhang, D.T. Tran, Mechanism and Solution for the Capacity Fading of Li/FeS_2 Battery, *J. Electrochem. Soc.* 163 (2016) A792–A797.
- [45] L. Chai, J. Wang, H. Wang, L. Zhang, W. Yu, L. Mai, Porous carbonized graphene-embedded fungus film as an interlayer for superior Li-S batteries, *Nano Energy* 17 (2015) 224–232.